Geophysical and Astrophysical Fluid Dynamics
Vol. 00, No. 00, Month 2009, 1–18

Generation of inertia-gravity waves in the rotating thermal annulus by a localised boundary layer instability

T. N. L. Jacoby†, P. L. Read†*, P. D. Williams‡ and R. M. B. Young†

†Atmospheric, Oceanic & Planetary Physics, Department of Physics, University of Oxford, Clarendon Laboratory, Parks Road, Oxford, OX1 3PU, UK

‡Department of Meteorology, University of Reading, Earley Gate, Reading, RG6 6BB, UK

(*28th December 2010*)

Waves with periods shorter than the inertial period exist in the atmosphere (as inertia-gravity waves) and in the oceans (as Poincaré and internal gravity waves). Such waves owe their origin to various mechanisms, but of particular interest are those arising either from local secondary instabilities or spontaneous emission due to loss of balance. These phenomena have been studied in the laboratory, both in the mechanically-forced and the thermally-forced rotating annulus. Their generation mechanisms, especially in the latter system, have not yet been fully understood, however. Here we examine short period waves in a numerical model of the rotating thermal annulus, and show how the results are consistent with those from earlier laboratory experiments. We then show how these waves are consistent with being inertia-gravity waves generated by a localised instability within the thermal boundary layer, the location of which is determined by regions of strong shear and downwelling at certain points within a large-scale baroclinic wave flow. The resulting instability launches small-scale inertia-gravity waves into the geostrophic interior of the flow. Their behaviour is captured in fully nonlinear numerical simulations in a finite-difference, 3D Boussinesq Navier-Stokes model. Such a mechanism has many similarities with those responsible for launching small- and meso-scale inertia-gravity waves in the atmosphere from fronts and local convection.

Keywords: Baroclinic instability; Baroclinic waves; Sloping convection; Inertia-gravity waves; Boundary layer

1 Introduction

Inertia-gravity waves (hereafter IGWs) are ubiquitous in planetary atmospheres and oceans. On Earth it is impossible to explain the atmosphere's global circulation without accounting for the momentum transport of IGWs. Furthermore, IGWs are thought to contribute to clear-air turbulence (Plougonven *et al.* (2003) and Knox *et al.* (2008)) and they may precipitate changes in the large-scale background flow (from one wavenumber mode to another, for instance) by noise-induced transitions (Williams *et al.* 2003). In the ocean, breaking internal gravity waves maintain the abyssal stratification and thus play a critical role in the thermohaline circulation. However, IGWs are poorly understood in terms of quantitative rules for their generation, especially far from topography.

IGWs have shaped the historical development of numerical weather prediction. Part of the problem is that IGWs span a range of scales both near and below the scale of the grids that many general circulation models (GCMs) use. It is thus especially difficult to separate genuine contributions due to IGWs from spurious grid-scale waves. The first numerical weather forecasts by Richardson (1922), done by hand, suffered from large and spurious IGW oscillations because of the use of unbalanced initial conditions. Later models set up the governing equations to be balanced, preventing the development of IGWs, and were more successful. Modern numerical weather forecasts do not filter IGWs from the governing equations, but are initialised in such a way as to prevent IGWs from appearing in subsequent iterations. Sub-gridscale IGWs are typically parameterized deterministically in numerical forecasts, but Williams *et al.* (2003) suggest that some phenomena may be captured only by stochastic parameterization or explicit representation.

As indicated above, the problem of IGW emission is intimately linked with the concept of balance. The general definition of a balanced flow given by McIntyre (2003) and others is one in which Rossby-Ertel

*Corresponding author. Email: p.read1@physics.ox.ac.uk

Geophysical and Astrophysical Fluid Dynamics
ISSN: 0309-1929 print/ISSN 1029-0419 online
DOI: 10.1080/03091920xxxxxxxxx

potential vorticity (hereafter REPV) inversion holds. That is, given the equation of state of the fluid, the boundary conditions and the REPV, all other dynamical information of the system can be extracted. The REPV can be considered a master scalar field, upon which we can apply some inversion operator and determine ρ, P, T, and $\mathbf{u}$. There are thus fewer degrees of freedom than in the most general flow regimes as variables are not fully independent but 'slaved' to one another by so-called *balance relations*, such as the geostrophic equation and the hydrostatic equation.

Evolving flows that remain balanced are said to lie on the slow manifold, although the existence of this manifold has been controversial. The slow manifold, first postulated by Leith (1980) and Lorenz (1980), is a hypothetical subspace embedded in the full phase space of a fluid-dynamical system on which trajectories can evolve without ever exciting fast modes (such as IGWs). The qualities of such a manifold have been debated since its inception. Lorenz (1980) argues that the manifold should exist, but that its stability is another matter. An unstable manifold will not have the attractor embedded in it. Indeed, Warn and Menard (1986) performed a series of numerical experiments from which they argued that if the slow manifold did exist, then it was likely to be unstable. They argued for a fuzzy slow subset of phase space, like a slow manifold but not well defined. This is called a 'slow quasi-manifold' (McIntyre 2003).

Recent work has shown that the slow manifold does not in fact exist for fluids (Ford *et al.* 2000), although it may do for certain low-dimensional systems such as the elastic pendulum (Lynch 2002). This is because real flows always emit some sound waves and IGWs through Lighthill radiation, although in some cases this radiation may be negligible. The non-existence of the manifold does not mean that we are unable to use the concept, however. By imposing balance conditions such as quasi-geostrophy on numerical weather forecasts, we are effectively forcing the model to evolve along a slow manifold. Such balance conditions are thus an approximation (in some cases a good one) to the actual evolution of the system.

In some recent work on IGW emission, Plougonven *et al.* (2003) analysed 224 radio soundings launched from ships in the North Atlantic in February 1997. They found that IGW activity in the upper troposphere and in the stratosphere was greatest close to the axis of the jet stream. Since they were measuring the waves nowhere near topography, they concluded that it was the jet regions themselves that were responsible for IGW emission. Specifically, they found that the two structural features of the jet flow which seemed to emit the most IGWs were the regions of maximum velocity and those in which the jet was strongly curved. They suggested that geostrophic adjustment was the cause of large amplitude IGW emission in the latter of these regions.

Zhang (2004) studied the generation of mesoscale ($\sim$ 100km) IGWs using a series of multiply nested numerical simulations with horizontal grid spacing 3.3km. He found that long-lived vertically propagating IGWs were generated at the exit region of the upper tropospheric jet-streak. His results were consistent with generation by spontaneous geostrophic adjustment. He hypothesised that baroclinic waves can emit IGWs from a continuously generated flow imbalance.

In the laboratory, Afanasyev (2003) showed that, in a non-rotating two-layer system, interfacial gravity wave emission appeared to be associated with a quadrapolar spatial distribution of vorticity. He suggested that IGWs were generated when a vortex quadrapole was emitted after two vortex dipoles collided. In later work, Afanasyev *et al.* (2008) did an experiment using a rotating tank of dense salt water. Fresh water injected at the surface produced a jet-like flow. A nearly-balanced flow was found to emit IGWs spontaneously when the Rossby radius of deformation was relatively small, such that the characteristics of baroclinic meanders matched the dispersion relation for the IGWs. Calculation of the vorticity from the velocity field confirmed that a quadrapolar vortical structure was responsible for IGW emission.

Lovegrove *et al.* (2000) and Williams *et al.* (2005) studied a rotating two-layer annulus laboratory experiment, which exhibited large-scale vortical modes generated by baroclinic instability, together with localised short-scale divergent modes. A sophisticated visualization method was used to observe the flow at very high spatial and temporal resolution. The Lighthill-type IGW emission mechanism was found to be an excellent predictor of the spatial locations of the short-wave emission observed in the laboratory. In a further analysis, Williams *et al.* (2008) found that the amplitude of the IGWs varied linearly with Rossby number, challenging the notion, suggested by several dynamical theories, that IGWs generated by balanced motion will be exponentially small.

The present paper studies the generation of IGWs by a localised boundary layer instability in the rotating

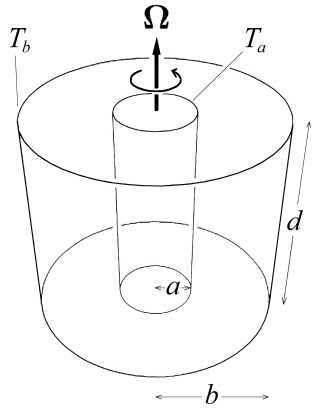

Figure 1. Schematic of the rotating thermal annulus.

thermal annulus. Section 2 describes numerical simulations using a 3D Boussinesq Navier-Stokes model. Section 3 examines the basic flow structures seen in the simulations (3.1), including the small-scale features near the inner cylinder (3.2), and compares them with laboratory measurements (3.3) by applying singular systems analysis (3.4) and the theoretical dispersion relation for IGWs (3.5). Section 4 applies a boundary layer instability theory to the system, by examining the thermal boundary layer (4.1) and its stability (4.2) in the context of the numerical simulations (4.3). Section 5 concludes the paper with a discussion.

2 The numerical model

We present analyses of data from a high-resolution numerical model of the thermally driven annulus and from a corresponding laboratory annulus experiment, both of which exhibit the emission of short period waves from the larger scale balanced flow. In particular, we use singular systems analysis (SSA) to show how the short waves are not emitted uniformly but at certain points during the drift cycle, and that the model and experiment are in good agreement as to when these emissions occur. We also examine the fast oscillations seen in the model runs in terms of the IGW dispersion relation, and show that they are consistent with being IGWs.

The annulus is composed of two vertical coaxial cylinders held at constant temperatures and closed at the top and bottom by rigid insulating endplates. The inner cylinder at radius $R = a$ is cooled (T_a) and the outer cylinder at radius $R = b$ is heated ($T_b > T_a$), and the working fluid fills the annular channel between the cylinders. The whole cavity rotates at a uniform rate, where the rotation vector $\mathbf{\Omega} = \Omega \mathbf{e}_z$ is anti-parallel to the gravity vector $\mathbf{g} = -g\mathbf{e}_z$ and coincides with the axis of the cylinders (Figure 1).

We use the Met. Office/Oxford Rotating Annulus Laboratory Simulation (MORALS) code. This solves the Navier-Stokes, continuity and heat transfer equations for a Boussinesq fluid rotating at angular velocity Ω, with a quadratic equation of state for density and constitutive relations for viscosity and thermal diffusivity. The integration scheme is finite-difference accurate to $\mathrm{O}(\Delta t^2)$, where Δt is the model timestep, using a Leapfrog scheme with a Robert-Asselin filter and discretised on an Arakawa-C grid. The grid is non-uniform, stretched in R and z in order to give three nodes within the boundary layers (grid spacing is as low as 0.4 mm in R and 0.5 mm in z). There are four prognostic variables: three velocity directions u (radial), v (azimuthal), and w (vertical) velocities /cm s^{-1}, and temperature T /°C. The fifth field is a kinetic pressure $\Pi = p/\rho_0$ /cm^2 s^2, which is diagnostic (calculated using a Poisson equation from the other four fields). All velocities are set to zero at the boundaries, and the temperature gradient is zero across the top and bottom boundaries.

The version of the model used here was originally developed by Farnell and Plumb (1975, 1976) and has been used for a variety of combined numerical and laboratory studies (James *et al.* 1981, Hignett *et al.* 1985, Young and Read 2008), demonstrating that the model successfully captures the principal flow regimes.

Following the established tradition, e.g. Fowlis and Hide (1965) and Hide and Mason (1975), the analysis

Parameter	Symbol	Value
Radius of inner cylinder	a	2.5 cm
Radius of outer cylinder	b	8.0 cm
Height	d	14.0 cm
Reference Temperature	T_0	20°C
Mean Density	ρ_0	$1.081\,\mathrm{g\,cm^{-1}}$
Rotation rate	Ω	$2.0302\,\mathrm{rad\,s^{-1}}$
Temperature of inner cylinder	T_a	15.01 °C
Temperature of outer cylinder	T_b	24.99 °C
Kinematic viscosity	ν	$0.02936\,\mathrm{cm^2\,s^{-1}}$
Thermal diffusivity	κ	$0.0012\,\mathrm{cm^2\,s^{-1}}$
Coefficient of cubic expansion	α	$3.93 \times 10^{-4}\ \mathrm{K^{-1}}$
Radial model resolution	N_R	32
Azimuthal model resolution	N_ϕ	128
Vertical model resolution	N_z	32
Model time step	Δt	0.002 s

Table 1. The parameters for the run.

of the flow for a given fluid in a fixed geometry is made with reference to two main parameters, the Taylor number Ta and the thermal Rossby number, given by

$$Ta = \frac{4\Omega^2(b-a)^5}{d\nu^2} \tag{1}$$

and

$$\Theta = \frac{gd\alpha(T_b - T_a)}{\Omega^2(b-a)^2}. \tag{2}$$

The latter can be interpreted in terms of a Rayleigh number, the Prandtl number ($\sigma = \nu/\kappa$) and the Taylor number defined above:

$$\Theta = \frac{4Ra}{\sigma Ta}. \tag{3}$$

The parameters listed in Table 1 are used. The fluid properties are for a water-glycerol mixture to compare with experimental data, e.g. Früh and Read (1997). The run was continued for 3000s, starting from a point at which the flow regime had already established itself (i.e: the model was started in the axisymmetric state, allowed to run for long enough (1000s) to establish a baroclinic wave pattern, and then the end point of this first run was used as the starting point of the next).

3 Results

3.1 *Basic flow structures*

From an initially perturbed axisymmetric flow, the system was found to develop a strong baroclinic wave with dominant wavenumber $m = 3$ which eventually equilibrated to an approximately steady amplitude. The azimuthally averaged flow is illustrated in Fig. 2, which shows (R, z) sections of the azimuthal velocity (a), temperature (b) and meridional streamfunction ψ (c). The temperature field shows the presence of well developed thermal boundary layers adjacent to each sidewall, with weak convective overshoot. In the interior the isotherms show complex sloping structures with stable stratification and weak slopes near the middle of the channel. The azimuthal velocity shows the usual reversal of flow between prograde motion at upper levels and retrograde at lower levels, with a double-jet structure at most heights consistent with

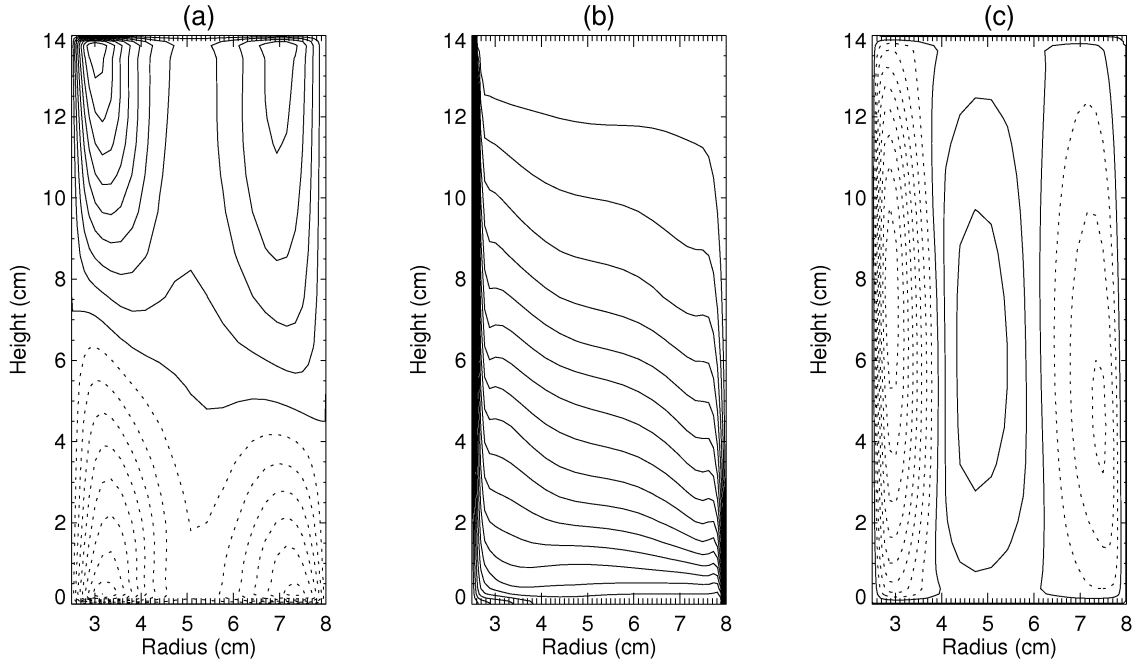

Figure 2. Maps in (R, z) of the azimuthally averaged, equilibrated $m = 3$ baroclinic wave flow, time averaged over 40 s, showing (a) azimuthal velocity, (b) temperature and (c) meridional streamfunction. Contour intervals are (a) 0.05 cm s^{-1} (< 0 dashed), (b) 0.5°C and (c) 0.01 cm^2 s^{-1}(< 0.02 dashed).

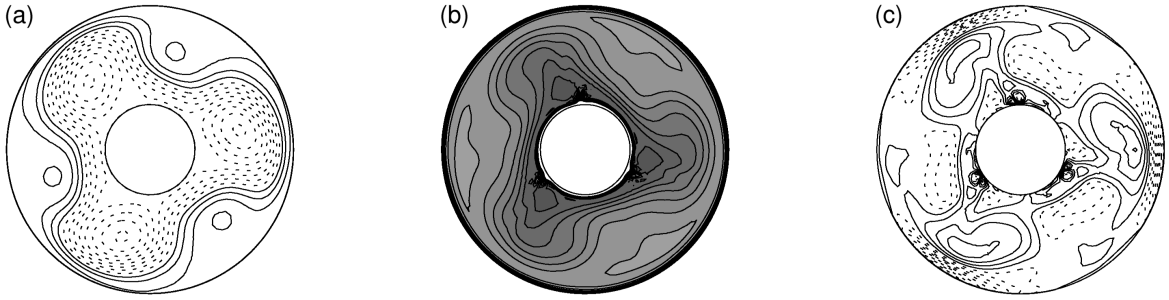

Figure 3. Maps in (R, ϕ) of the equilibrated $m = 3$ baroclinic wave flow at mid-level, showing (a) kinetic pressure (p/ρ), (b) temperature and (c) vertical component of relative vorticity. Contour intervals are (a) 0.2 cm^2 s^{-1} (< 0 dashed), (b) 0.25°C and (c) 0.1 s^{-1}(< 0 dashed).

the presence of a large-scale wave. The meridional streamfunction exhibits three basic cells, representing thermally direct circulation in the two sidewall boundary layers and a thermally indirect 'Ferrel' cell in mid-channel. In all respects, this is largely consistent with previous simulations of baroclinic annulus wave flows (James *et al.* 1981, Hignett *et al.* 1985).

Horizontal flow fields (Fig. 3) are also consistent with this picture. The pressure and temperature fields (e.g. Fig. 3(a) and (b)) exhibit a large amplitude, regular $m = 3$ flow pattern with a strong, well-defined meandering zonal jet and thermal front connecting the inner and outer sidewall boundaries. The vorticity field at mid-level (Fig. 3(c)) is dominated by strong cyclonic features in mid-channel and much weaker anticylonic features in the accompanying ridge in kinetic pressure. Near the inner cylinder, however, there is an indication of some intense, small-scale features, close to where the meandering zonal jet starts to move away from the inner cylinder itself. These features were seen to be strongly time-dependent and also have a clear signature in the temperature field in Fig. 3(b). They are considered in more detail in the next subsection.

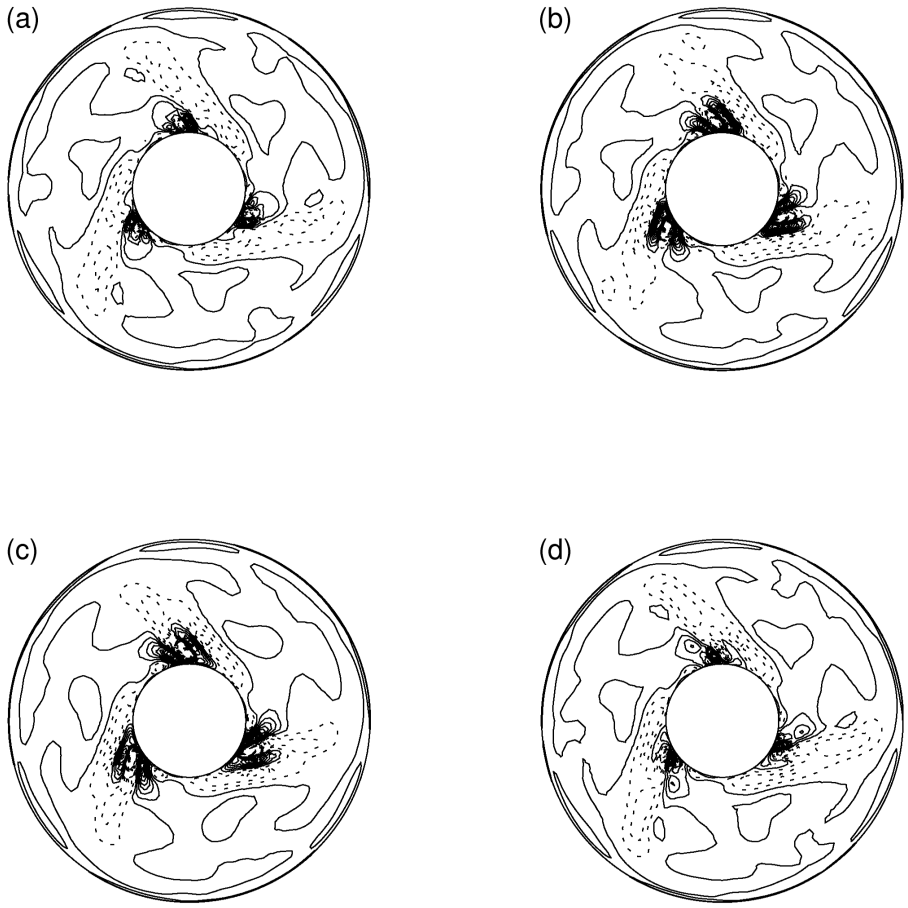

Figure 4. Maps in (R, ϕ) of the equilibrated $m = 3$ baroclinic wave flow at mid-level, showing contours of horizontal divergence at mid-level every 12 s. Contour interval is 0.025 s^{-1}(< 0 dashed).

3.2 *Small-scale features near the inner cylinder*

The intense, small-scale features mentioned above were found to vary strongly on timescales of a few tens of seconds. Although they occur on scales comparable with the resolution of the model itself, they show fairly clear, cyclic behaviour that suggests a physical, rather than a purely numerical, origin. The features were particularly prominent in fields of horizontal divergence, indicating a possible link to non-geostrophic dynamical phenomena. Fig. 4 shows a sequence of horizontal divergence fields at mid-level, separated at intervals of 12 s. At the location of the intense vorticity features in Fig. 3(c), some very strong alternating centres of local divergence and convergence are apparent with sloping linear extensions into the interior flow. As time progresses, these small centres of divergence and convergence progress retrograde in a wavelike manner, following a cycle with a period of around 40 s. A thin tongue of negative divergence is also seen to extend from the inner cylinder across the entire annular channel along a path sloping prograde with radius.

These features also have a signature in the temperature field (Fig. 5), where prominent oscillations in very small, radially-oriented filamentary structures can be seen close to the inner cylinder. These oscillations (also with a period $\sim$ 40 s) also affect the temperature structure on larger scales, with a corresponding weak modulation of the temperature field near mid-channel.

A clearer impression of the three-dimensional structure of these features in temperature and horizontal divergence can be gained from (ϕ, z) sections through the flow at radii close to the inner cylinder. Fig. 6 shows a sequence of temperature contour maps (Fig. 6(a), (c) and (e)) and horizontal divergence (Fig. 6(b), (d) and (f)) at $R = 3.167$ cm, just 6.67 mm away from the inner sidewall boundary and separated in time by 16 s. This reveals that the intense, small-scale features seen in the horizontal section extend over much of the depth of the annular channel, but with a complex, wave-like structure with phase lines that

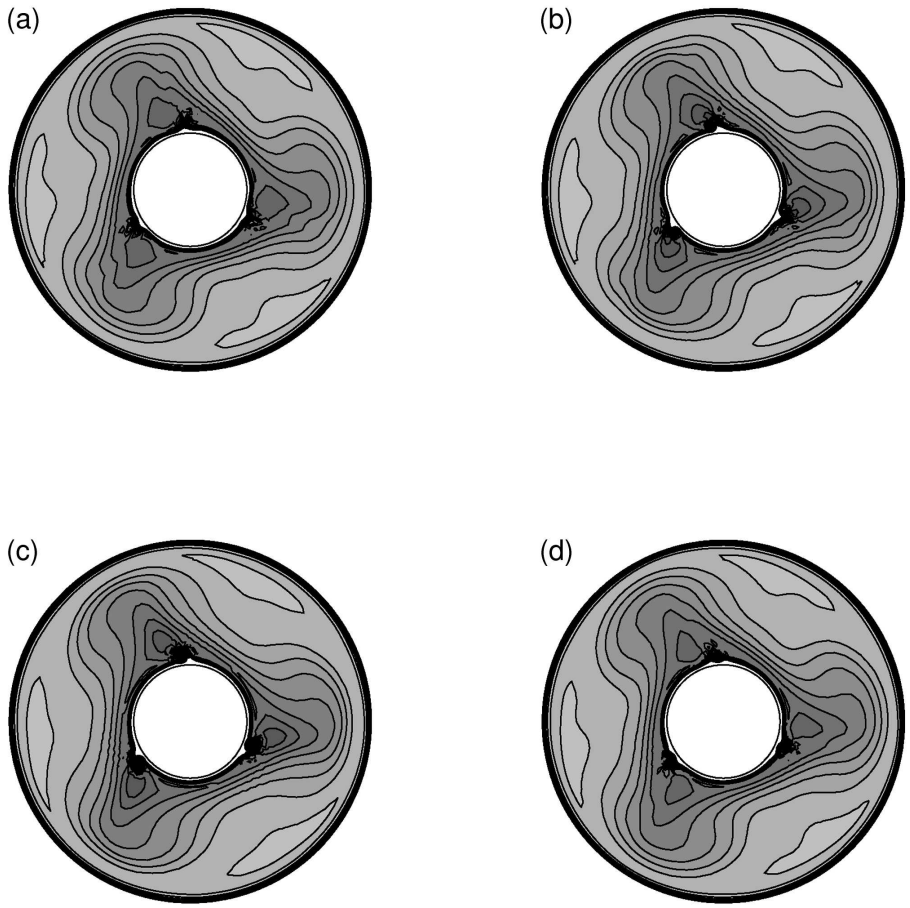

Figure 5. Maps in (R, ϕ) of the equilibrated $m = 3$ baroclinic wave flow at mid-level, showing contours of temperature at mid-level every 12 s. Contour intervals are 0.25°C.

tilt retrograde with height. As time progresses, the phase lines in divergence propagate downwards, and the amplitude of the oscillation is modulated in both z and ϕ with maximum amplitude around or just below mid-depth.

The temperature contours in Fig. 6(a), (c) and (e) show the small-scale features to be superimposed upon gentle undulations of the temperature field associated with the large-scale $m = 3$ baroclinic wave, forming prominent localised peaks and troughs in the vicinity of the maxima and minima in divergence. As time progresses, the sharp elevations of the mid-level temperature contours are seen to lift and overturn, giving the clear impression of a breaking wave event before subsiding towards the end of the cycle (Fig. 6(e)). The location of these 'wave breaking' events can be seen with respect to the large-scale baroclinic wave in Fig. 6(a), (c) and (e), which also shows background shading representing the eddy pressure field ($p' = p - \overline{p}$). The small scale features are evidently aligned with the tilt of the eddy pressure field on the trailing side of the high pressure ridge (noting that the wave propagates slowly prograde, i.e. towards increasing azimuth θ) in the lower 2/3 of the height domain.

The radial structure of these small-scale features as they propagate downwards in the flow can be seen in (R, z) sections in Fig. 7, taken at a point in azimuth through the centre of the disturbance shown in Fig. 6 at intervals of 12 s. These snapshots clearly show a periodic structure in $\nabla_h.\mathbf{u}$ growing away from the inner sidewall as it propagates downwards, growing in amplitude below $z = 10$ cm until around $z = 4$ cm, below which it appears to decay and disappear. The corresponding disturbances in T (not shown) also exhibit evidence of overturning events emerging out of the strong thermal gradients in the thermal boundary layer adjacent to the inner sidewall.

These results would all appear to be consistent with the development of an intense, roll-like instability within the thermal boundary layer adjacent to the inner sidewall, forming a spatially periodic structure that propagates vertically downwards but with complex phase structure that is inclined with respect to the

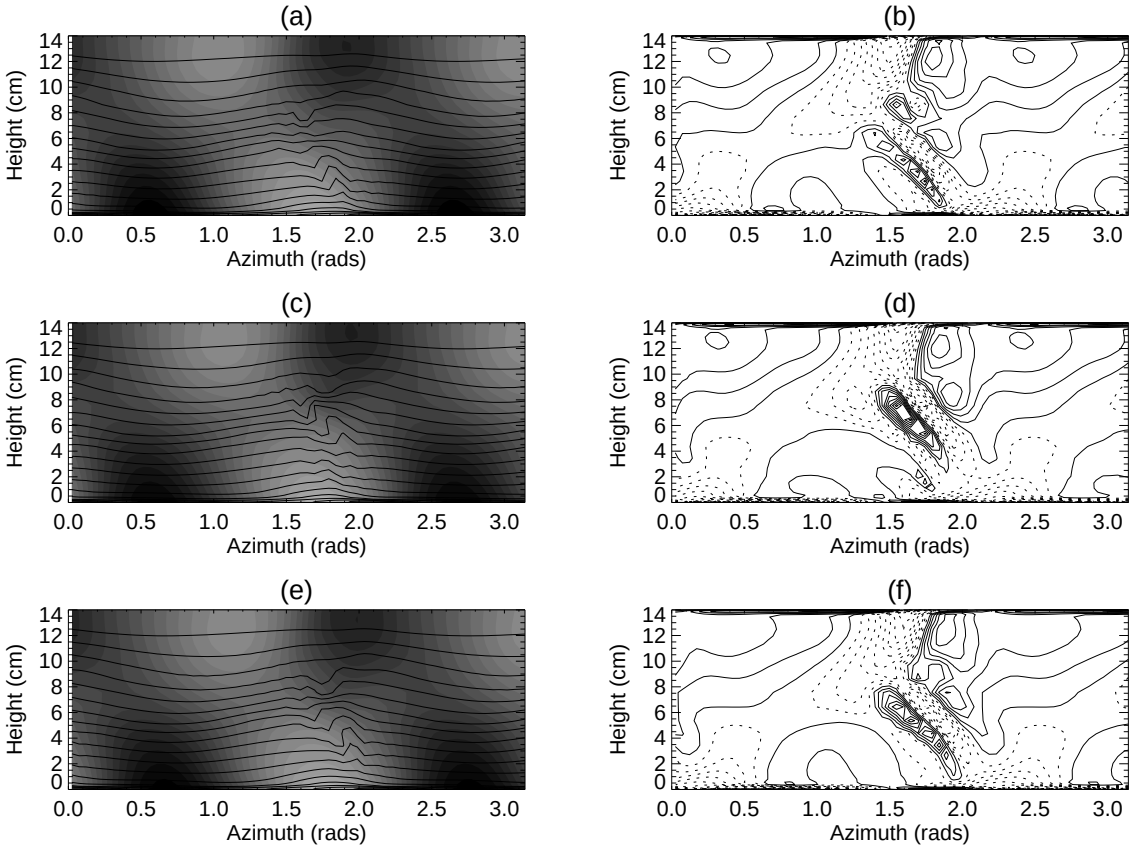

Figure 6. Maps in (ϕ, z) of the equilibrated $m = 3$ baroclinic wave flow at $R = 3.167$ cm over π radians of azimuth, showing contours of (a, c & e) temperature superposed over shaded levels of eddy pressure, p' and (b, d & f) horizontal divergence. Each row is separated from the next by $\delta t = 16$ s and contour intervals are 0.5°C (a, c, e) and 0.025 s^{-1}(< 0 dashed).

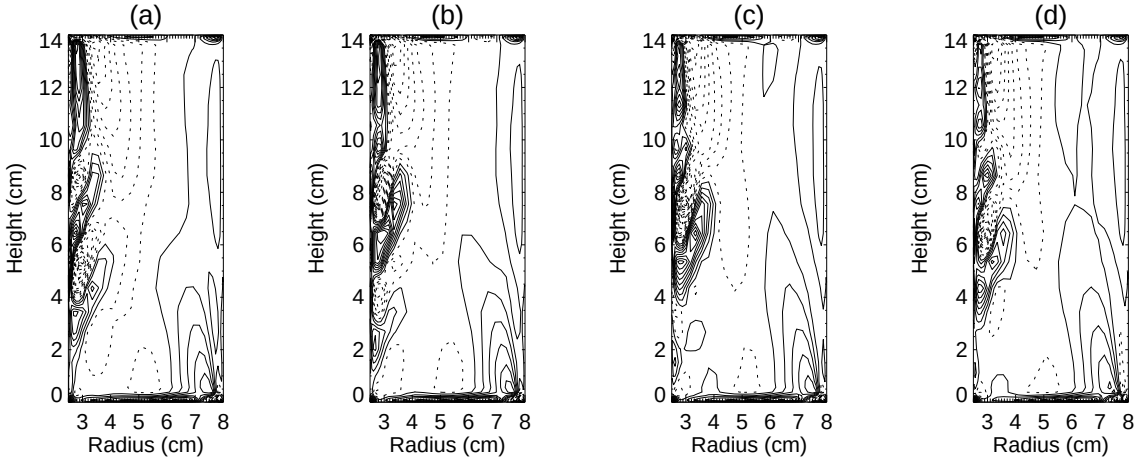

Figure 7. Maps in (R, z) of the equilibrated $m = 3$ baroclinic wave flow at fixed azimuth through the main peak of activity in the divergence field near the inner cylinder, showing contours of horizontal divergence at intervals of 12 s. Contour intervals are 0.025 s^{-1}(< 0 dashed).

horizontal and aligned approximately with the axis of p' within the main baroclinic wave. The azimuthal location of this propagating structure is evidently determined by the structure of the large-scale baroclinic wave, since it is also observed slowly to migrate azimuthally around the annulus in phase with the drift of the baroclinic wave itself. In fact it appears to align closely to where the downward vertical velocity within the baroclinic wave reaches a maximum close to the inner boundary, suggesting that the superposition of this downwards flow results in an azimuthal modulation of the vertical flow in the thermal boundary layer that focusses small-scale instabilities into the location where $|w|$ is a maximum.

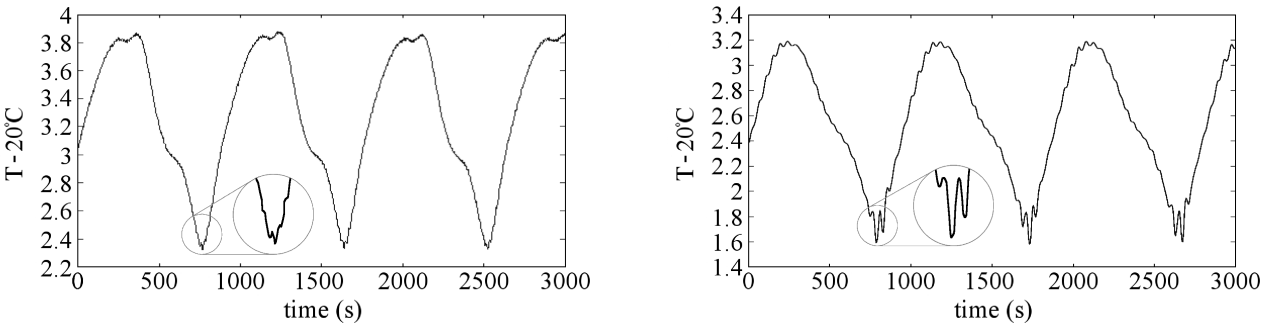

(a) Experimental data. (b) MORALS

Figure 8. Temperature anomaly (T - 20°C) versus time.

While this appears to represent a physically plausible dynamical phenomenon within the energetic inner sidewall boundary layer, it is important to examine critically (a) whether there is any experimental evidence for this phenomenon in laboratory measurements, and (b) whether its characteristics can be accounted for by dynamical theory. In the next subsection, therefore, we extract timeseries of temperature and other variables in a form that may be compared with the available experimental measurements of Read (1992). These results are further considered in Section 4 with reference to some published theoretical analyses of generic instabilities of vertically-oriented thermal boundary layers.

3.3 *Comparison with laboratory measurements*

The small scale nature of the phenomenon described in the previous section and its concentration into the very thin thermal boundary layer adjacent to the inner cylinder makes it relatively inaccessible for direct experimental measurement. It is not surprising, therefore, that there appear to be no previously published reports of this kind of instability in thermal annulus experiments. In a study aimed at applying novel timeseries analysis methods to experimental measurements, Read (1992) reported evidence of small-scale, high frequency oscillations present in the temperature signal from a fully-developed, azimuthally drifting baroclinic wave that he speculated might represent propagating IGWs from an undetermined source. In this subsection, therefore, we consider whether waves originating from the boundary layer oscillations found in the present simulations might be consistent with the high frequency oscillations found by Read (1992).

Figures 8(a) and 8(b) show extracts from timeseries of temperature about a mean value of 20°C (i.e. $T - 20$°C) for the laboratory experiment of Read (1992) and from our numerical model, both taken at a single point in the annular domain at mid radius and mid height. Both series exhibit a broadly similar low frequency oscillation structure associated with the drift of the main baroclinic wave, with a drift period ~ 950s. The amplitudes of the baroclinic waves in both experiment and simulation are approximately 1.5°C peak to peak. In addition, there also appear to be smaller amplitude short period oscillations present in both timeseries, though of somewhat differing amplitudes and frequencies. The periods of these fast oscillations are ~ 50s and ~ 20s in the model and experiment respectively, and their amplitude seems rather larger in the simulation than in the experiment. Nevertheless, the oscillations seem to share sufficient qualitative similarities to warrant further investigation.

3.4 *Singular systems analysis applied to our data*

Singular Systems Analysis (SSA) is a method of optimally decomposing a time series of data into its mutually independent components via the eigenvectors of a covariance matrix formed from that data. Oscillatory signals in the data show up as pairs of eigenvectors approximately $\pi/2$ out of phase and with similar eigenvalues (Ghil *et al.* 2002). For a review of SSA as a method of analysing chaotic data see Broomhead and King (1986) or Read (1992).

In the following analyses the data vectors are the time series of temperature anomaly shown in Fig-

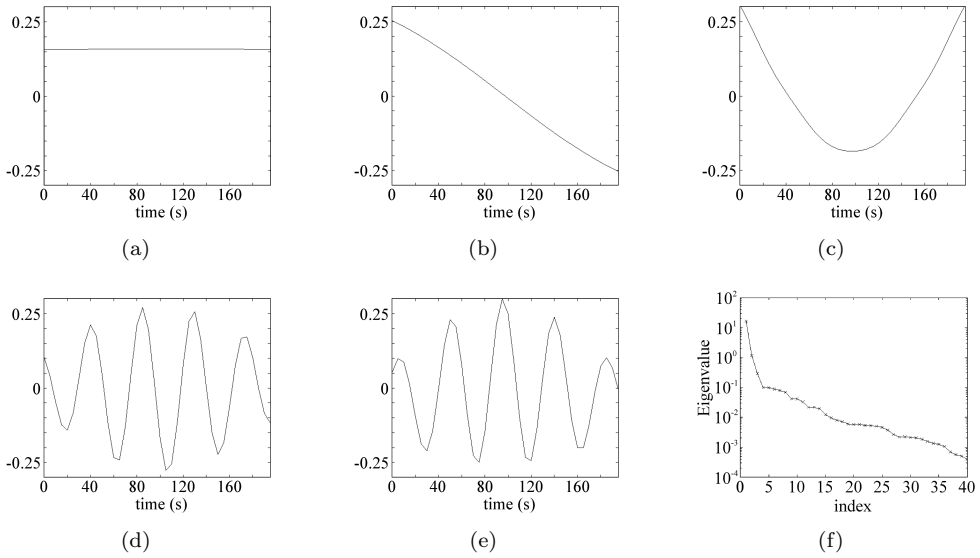

Figure 9. (a) - (e) Profiles of the first five eigenvectors for SSA done on the temperature perturbation generated by the MORALS model. (f) Shows the singular spectrum from the same analysis with index on the x axis and log eigenvalue on the y axis.

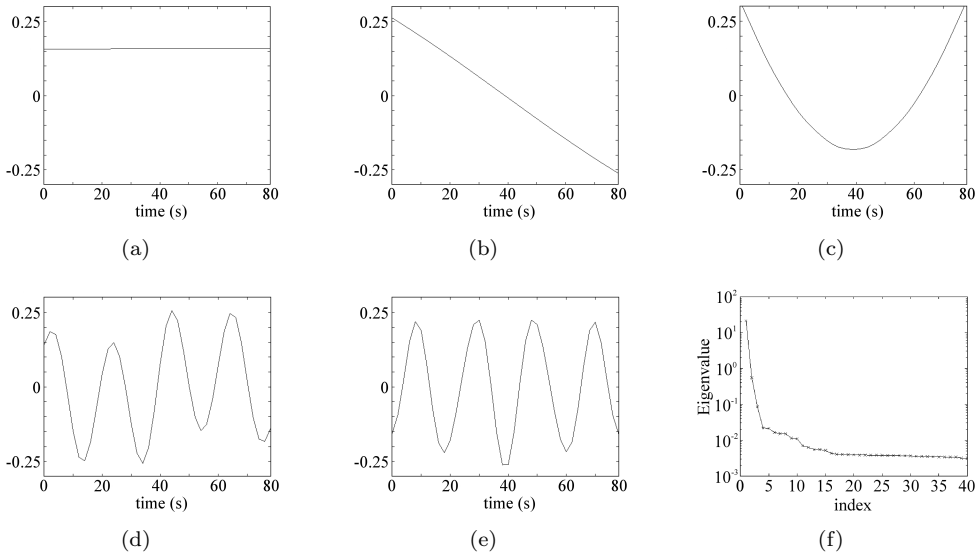

Figure 10. (a) - (e) Profiles of the first five eigenvectors for SSA done on the temperature perturbation time series from Read (1992). (f) Shows the singular spectrum from the same analysis with index on the x axis and log eigenvalue on the y axis.

ures 8(a) and 8(b). Note that due to the different periods of the short waves in each case we use window lengths of 200 s and 80 s in constructing the covariance matrices from the MORALS and laboratory data respectively.

Figure 9 shows the result for the numerical data. We note that eigenvalues 4 and 5 are approximately equal, and that the form of eigenvectors 4 and 5 is sinusoid-like while the first three are more Legendre-like. We also note that eigenvectors 4 and 5 are in approximate phase quadrature. These two eigenvectors represent the principal short period modes seen in both timeseries. Indeed, we see approximately four peaks in each vector, corresponding to a wave period of ~ 50s. The corresponding analysis of the lab data is shown in Figure 10. Again the travelling short waves show up in eigenvectors 4 and 5, as found by Read (1992), though this time with the shorter window we see their period to be ~ 20s.

Figure 11 shows Principal Components (PCs) of the first and fifth eigenvectors, projected onto the original laboratory time series of Figure 8. The PC of the first eigenmode gives a smoothed version of the original, that is the profile of the low frequency baroclinic wave. The modulus of the fifth PC gives an indication of the intensity of the short waves at any given time. From this we see both that the intensity of

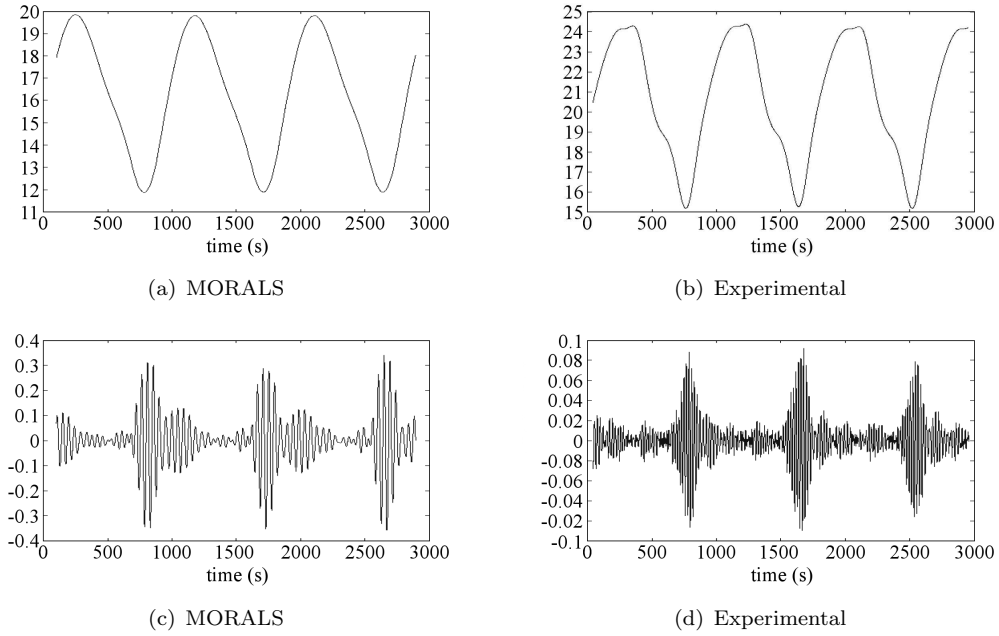

(a) MORALS (b) Experimental

(c) MORALS (d) Experimental

Figure 11. (a) and (b) Projections of the first eigenvector of each SSA analysis onto the time series shown in Figures 8(b) and 8(a) respectively; (c) and (d) projections of the fifth eigenvectors onto the series.

the short waves in the laboratory flow is less than that of those seen in the simulation, and that the intensity varies by approximately an order of magnitude during the drift period. However, it is also noteworthy that the qualitative form of PC 5 is largely the same in both cases, and that short wave activity reaches a maximum and minimum at approximately the same points in the drift cycle.

We see, therefore, that both the numerical model and the laboratory experiment exhibit short period waves within a large-scale baroclinic wave flow. The form and period of the baroclinic flow is in good agreement in both experiments and simulation, while the periods of the short waves as measured in the annulus frame are of the same order of magnitude, although the amplitude and period of the short waves is rather greater in the numerical model. These short waves are not present continuously but peak at certain points in the drift cycle. Moreover, the points in the cycle at which they occur are approximately the same in both the numerical and laboratory data. It should be noted that when the experimental data was first analysed, Read was concerned that the short waves seen might have been excited by interactions with the thermocouple ring. The presence of the waves in the numerical model, which has no such obstacle to the flow, provides evidence of high frequency wave generation associated with baroclinic instability alone. Conversely, this agreement between the model and laboratory data provides strong evidence that the fast oscillations seen in MORALS are physical, rather than numerical, in origin.

3.5 *Inertia-gravity waves*

Both experimental and simulated timeseries exhibit evidence for high frequency oscillations that appear to propagate across the annulus from a site of origin close to the inner cylinder. In investigating this phenomenon further, it is of interest to consider whether this might represent a travelling wave disturbance of generic form. The results of Sections 3.1 and 3.2 indicate that, unlike the large-scale wave flow which shows up strongly in vertical vorticity but hardly at all in horizontal divergence fields, the high frequency disturbances are at least as strong in $\nabla_h \cdot \mathbf{u}$ as in vorticity fields. This is particularly evident in the intense 'wavemaker' regions close to the inner sidewall. Such a strongly divergent flow is suggestive of highly ageostrophic wave motion characteristic of IGWs and so we now consider this possibility with reference to the dispersion relation and other properties of IGWs.

Inertia-gravity waves in a medium in which there is a mean zonal flow of velocity $U\mathbf{i}$ and Brunt-

Vaïsälä frequency N obey the dispersion relation:

$$\omega = \left\{ \frac{f^2 m^2 + N^2(k^2 + l^2)}{k^2 + l^2 + m^2} \right\}^{1/2} - Uk \tag{4}$$

where $f = 2\Omega$, k l and m are zonal, radial and vertical wavenumbers and ω and U are measured *with respect to the rotating frame*. The first term on the rhs is the zero-mean-flow IGW dispersion relation and the second represents the Doppler shift of the wave. We can estimate the three components of the wave vector (k, l, m) from horizontal and vertical plots of one of the variables in the numerical simulation, say temperature. Figure 5 shows the temperature in horizontal slices near mid height. From this we can estimate

$$k \sim \frac{2\pi}{0.74\text{cm}} \qquad \text{and} \qquad l \sim \frac{2\pi}{1.0\text{cm}}$$

Similarly from Fig. 6 we estimate

$$m \sim \frac{2\pi}{3.0\text{cm}} \qquad \text{and} \qquad \frac{\partial T}{\partial z} \sim \frac{3\text{K}}{5\text{cm}}$$

suggesting $N \sim 0.5$ rad s^{-1}. We estimate $U \sim 0.02$cm/s by taking time and azimuthal averages of the zonal velocity.
From equation (4), therefore, we obtain $\omega \approx 0.33$ rad/s indicating an intrinsic period ≈ 19 s. This is close to the observed value of ~ 20s in the laboratory and is of the same order of magnitude as that seen in MORALS (~ 50s). We note, however, that the value for intrinsic period estimated here is quite sensitive to the actual values of U and k chosen. We nevertheless conclude that the short period waves found in the simulated flow are not inconsistent with the IGW dispersion relation, given a plausible Doppler shift. Note also that a full treatment of this subject should include viscosity and thermal diffusivity in the dispersion relation, although this is beyond the scope of this paper.

4 Boundary layer instability

The numerical simulations described above present evidence of particular regions of the boundary layer close to the inner cylinder acting as an energetic 'wavemaker', launching IGWs into the interior of the annular domain where they may be detected experimentally. This would suggest the possibility of an instability within the thermal boundary layer flow as the origin of the oscillations observed in the MORALS simulations. Accordingly, we now go on to consider what kind of instability might be responsible for this behaviour, and to compare the results of published instability analyses with our simulations to evaluate their relevance.

4.1 *The thermal boundary layer*

Gill (1966), Gill and Davey (1969) and Daniels (1985) analysed instabilities arising in the vertical boundary layer of a buoyancy-driven, two-dimensional system. Figure 12 shows a schematic outline of the system considered. A fluid of kinematic viscosity ν, thermal diffusivity κ and coefficient of cubical expansion α is bounded at $x = 0$ by an infinite vertical plane. The plane is subject to a constant vertical temperature gradient G, and is held at a fixed horizontal temperature difference ΔT with respect to fluid far in the interior. They consider a thermal boundary layer of thickness $\sim l_B$ in which vertical velocities are significant.

Gill and Davey (1969) considered the stability of a basic two-dimensional, steady flow of this type to two-dimensional disturbances within linearised forms of the azimuthal vorticity and heat advection equations.

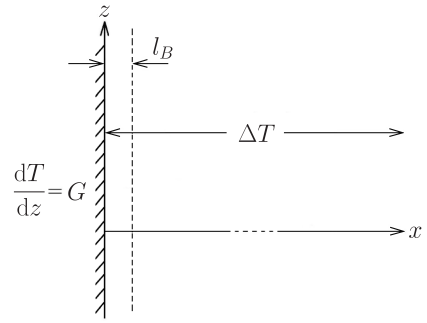

Figure 12. The system of Gill and Davey. A fluid is bounded at $x = 0$ by an infinite plane whose temperature varies linearly with height. There is a constant horizontal temperature difference, ΔT, between the plane and fluid a long way away and a boundary layer of thickness l_B is established in which vertical velocity is significant.

These were derived earlier by Gill (1966), and were nondimensionalised assuming

$$u \sim U, \qquad w \sim W, \qquad \psi \sim \Psi \qquad \frac{\partial T}{\partial z} \sim G$$

where ψ is the meridional streamfunction. By introducing a length scale, l_B, for the thickness of the thermal boundary layer, where $l_B \ll H$, and assuming $\Delta T/l_B \lesssim G$, an advective-diffusive balance in the heat equation implies $\Psi \sim \kappa \Delta T/G l_B$. A buoyancy-viscous balance in the vorticity equation then implies

$$l_B^4 \sim \nu\kappa/N^2 \qquad \text{where} \qquad N = (\alpha g G)^{1/2} \tag{5}$$

and hence

$$W \sim g\alpha\Delta T/(\sigma^{1/2} N) \tag{6}$$

All quantities were non-dimensionalised using $l_B\sqrt{2}$, W, and ΔT as units of length, velocity and temperature[1]. The surd in the length scale is to ensure consistency with earlier work and to simplify the equations. Defining a Reynolds number $Re \equiv W l_B \sqrt{2}/\nu$ and letting the non-dimensional streamfunction and temperature be φ and ϑ respectively, the time dependent vorticity and heat equations can be written in non-dimensional form

$$Re \frac{D}{Dt^*} \nabla^2 \varphi \;=\; 2\vartheta_{x^*} \;+\; \nabla^4 \varphi \tag{7}$$

$$\sigma Re \frac{D}{Dt^*} \vartheta \;+\; 2\varphi_{x^*} \;=\; \nabla^2 \vartheta \tag{8}$$

where

$$\nabla \;\equiv\; \frac{\partial}{\partial x^*} \;+\; \frac{\partial}{\partial z^*}$$

and

$$\frac{D}{Dt^*} \;\equiv\; \frac{\partial}{\partial t^*} \;-\; \varphi_{z^*} \frac{\partial}{\partial x^*} \;+\; \varphi_{x^*} \frac{\partial}{\partial z^*}$$

[1]In our notation, an asterisk, as x^*, denotes a dimensionless quantity whilst dimensional quantities are unstarred. We do this to maintain consistency throughout this paper. Gill (1966) and Gill and Davey (1969) use the star notation the other way round.

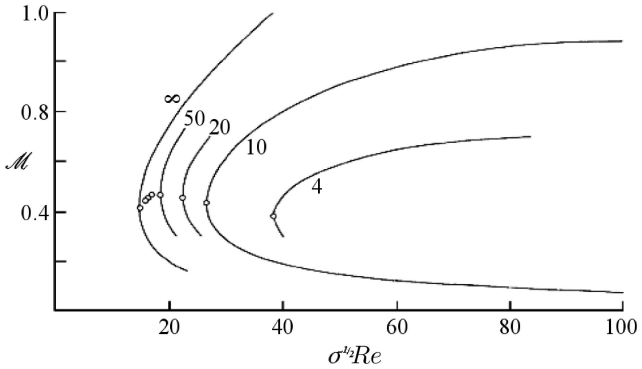

Figure 13. Gill and Davey's neutral stability curves for Prandtl numbers $\sigma = 4$, 10, 20, 50 and ∞, adapted from their 1969 paper. The circles are critical values for $\sigma = 100$, 200, and 400.

Steady state solutions (Gill 1966) to these equations are obtained

$$w^* = \mathscr{W}(x^*) = e^{-x^*} \sin x^* \tag{9}$$

$$\vartheta = \Theta(x^*) = e^{-x^*} \cos x^*. \tag{10}$$

Gill and Davey examined the stability of this steady flow to small amplitude perturbations, φ_{pert} and ϑ_{pert} applied to the streamfunction and temperature of the form

$$\varphi_{\text{pert}} = \Re\{\phi(x^*) \exp(i\mathscr{M}(z^* - \mathscr{C}t^*))\} \tag{11}$$

$$\vartheta_{\text{pert}} = \Re\{\theta(x^*) \exp(i\mathscr{M}(z^* - \mathscr{C}t^*))\} \tag{12}$$

with boundary conditions

$$\phi = \phi' = \theta = 0 \qquad \text{at} \qquad x^* = 0$$

and

$$\phi, \theta \to 0 \qquad \text{as} \qquad x^* \to \infty.$$

4.2 *Neutral stability curves*

Gill and Davey solved the linearised governing equations for φ_{pert} and ϑ_{pert} numerically in order to produce neutral stability curves (Fig. 13) for which $\Im\{\mathscr{M}\mathscr{C}\}$ is zero. The point to note is that to the left of a curve the fluid is stable, and to the right it is unstable to this instability. The circles are critical values, representing values of the Reynolds number above which the fluid can be unstable to disturbances of vertical wavenumber $\mathscr{M}$. From this figure, it is clear that the wavenumber of initial instability is not very sensitive to Prandtl number, although the critical Reynolds number itself does depend on σ.

4.3 *Application to MORALS simulations*

The boundary layer system outlined above is irrotational. Before applying the theory to the rotating annulus, we look at whether such a theory could be appropriate. Considering the MORALS run defined by the parameters listed in Table 1 and using the approximate value of buoyancy frequency from section 3.5, equation 5 gives $l_B = 1.1$ mm. Defining a local Rossby number in the boundary layer to be

$$Ro_{\text{local}} = \frac{\sqrt{u^2 + v^2}}{2\Omega l_B}$$

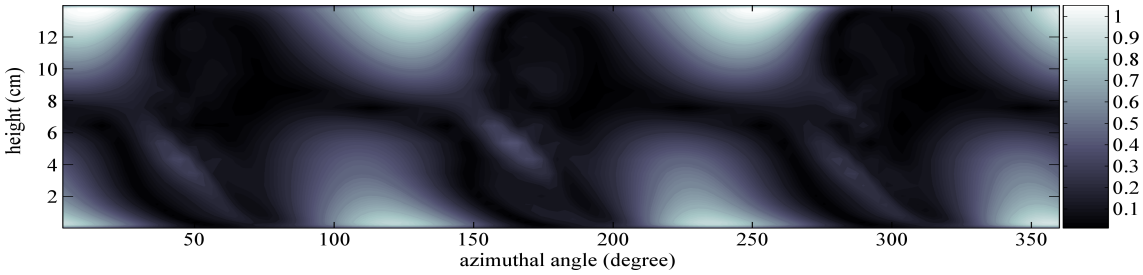

Figure 14. Local Rossby number at radius 2.6521 cm. The data are shown at time 800 s.

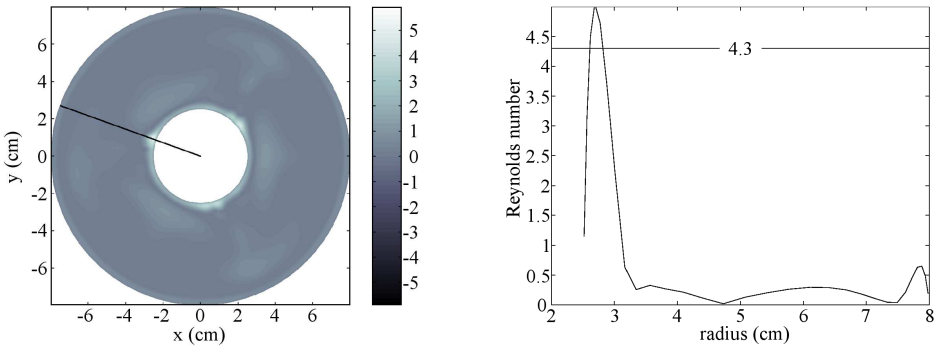

(a) Local Reynolds number at mid height in the annulus.

(b) Local Reynolds number versus radius along the line shown.

Figure 15. Local Reynolds number during the MORALS run. The data is taken at time 800s. The maximum value of reynolds number is 5.05.

we see that peak $Ro_{\rm local}$ is O(1) near to the inner cylinder (Figure 14). We therefore suggest that whilst rotation may be important, it is unlikely to be the dominant force in the boundary layer. However, the potential modifying influence of rotation on the instability analysed by Gill and Davey should be considered in more detail in future work.

For comparison with the theory, we let $\Delta T = 5°$C (i.e: half the horizontal temperature difference between the inner and outer walls), which gives (from eqn. 6) $W = 0.81$ cm s^{-1}. Interpolating Gill and Davey's results for critical Reynolds number against Prandtl number gives $Re_{\rm crit} = 4.30$. An estimate of the local Reynolds number can be defined from the simulated velocity fields as

$$Re_{\rm local} \equiv \frac{|w| l_B \sqrt{2}}{\nu} = 5.30 \cdot |w|. \tag{13}$$

Where $|w|$ is measured in cm s^{-1}. Figs. 15(a) and 15(b) show the variation of this quantity within the flow, from which we see that not only is the critical Reynolds number exceeded, but moreover that it is exceeded just in the place where the 'wavemaker' disturbances are seen to develop in the numerical simulations.

The boundary layer instability theory makes predictions about the wavelength and frequency of the most unstable waves for which $Re_{\rm local} > Re_{\rm crit}$. Gill and Davey (1969) give a look up table for nondimensional wavenumber and velocity in terms of the Prandtl number of the fluid. For a fluid of Prandtl number 24.5 we interpolate these to be

$$\mathscr{M} = 0.46 \qquad \text{and} \qquad \mathscr{C} = 0.44$$

Re-dimensionalising, we get

$$\text{vertical wavelength} \sim 2.1\,\text{cm},$$

and including the Doppler shift by the zonal mean flow as before according to $\omega_{\text{Doppler}} = \omega - Uk$ we get

$$\text{intrinsic period} \sim 7.1\,\text{s}.$$

These are the same order of magnitude as the values we estimated in the previous section.

We repeated the above analysis for results obtained from a MORALS run using a Prandtl number 13.5 fluid with other properties and parameters the same. The flow structure was broadly similar with wavemaker regions close to the inner cylinder, though the baroclinic wave was of mode four. Again we saw how the Reynolds number criterion was broken only in these wavemaker regions.

5 Summary and discussion

We have examined short-period waves in high-resolution numerical simulations, using a Navier-Stokes model of the rotating thermal annulus. We have compared the waves with the corresponding observations from earlier laboratory experiments. Singular systems analysis (SSA) was applied to the experimental and numerical data, to show how the short waves in both cases are not present continually but appear only at certain times during the drift cycle. The wave characteristics are found to be broadly consistent between the model and experiment. In the model, the short-period features are particularly prominent in the horizontal divergence field, indicating a link to non-geostrophic dynamical phenomena. The features are consistent with the theoretical dispersion relation for Doppler-shifted inertia-gravity waves.

The numerical simulations suggest that particular regions of the boundary layer, close to the inner cylinder, act as an energetic wavemaker. The wavemaker launches small-scale inertia-gravity waves into the geostrophic interior of the annular domain, where they have been detected experimentally in previous studies. This suggests the possibility of an instability within the thermal boundary layer flow as the origin of the oscillations observed in the simulations. Indeed, we find that not only is the critical Reynolds number for a particular boundary-layer instability exceeded, but moreover that it is exceeded just in the place where the wavemaker disturbances are seen to develop in the numerical simulations. We conclude that the short-period waves are consistent with being inertia-gravity waves generated by a localised instability within the thermal boundary layer, the location of which is determined by regions of strong shear and downwelling at certain points within a large-scale baroclinic wave flow.

The thermal boundary layer instability studied herein has many similarities with some of the mechanisms responsible for launching inertia-gravity waves of meteorological and oceanographic importance. Specifically, the laboratory mechanism appears to have much in common with the mechanisms by which small- and meso-scale inertia-gravity waves are launched from fronts and local convection in the atmosphere and ocean. We speculate that the generation of inertia-gravity waves through this particular boundary instability may potentially offer insights into their generation in more general flow configurations, wherever vertical gradients of temperature are associated with localised convective regions in which the vertical velocity is large.

As discussed above, inertia-gravity waves in the thermal annulus appear to be generated by wavemakers associated with a thermal boundary layer instability. However, it remains unclear whether there is a plausible interpretation in terms of the instability causing loss of balance and the concomitant emission of inertia-gravity waves through geostrophic adjustment (or spontaneous adjustment). This possibility is especially pertinent, because spontaneous-adjustment emission has been successfully invoked to explain inertia-gravity wave generation at the internal interface in the two-layer, mechanically forced, isothermal analogue of the thermally forced annulus. Although this topic is an attractive candidate for future work, the fundamentally small-scale nature of the phenomenon, and its concentration into a very thin thermal boundary layer, mean that progress is likely to require numerical simulations as well as direct experimental measurements. These numerical simulations should also determine where in parameter space the boundary layer instability is deactivated. A naïve theory in which it is assumed that $\partial T/\partial z \propto \Delta T$ suggests that local Reynolds number might scale as $\Delta T^{1/4}$, although we have been unable to confirm this as yet, and we suggest that this be investigated further beyond this paper.

Acknowledgements

TNLJ, RMBY and PDW are grateful to the UK Natural Environment Research Council for their support of this work via research studentships (references: NER/S/A/2006/14177 and NER/S/A/2005/13667) and Fellowship (reference: NE/D009138/1), respectively. PDW also acknowledges funding through a University Research Fellowship from The Royal Society (reference: UF080256).

References

Afanasyev, Y.D., Spontaneous emission of gravity waves by a stratified fluid: laboratory experiments. *Geophys. Astrophys. Fluid Dyn.* 2003, **97**, 79–95.

Afanasyev, Y.D., Rhines, P.B. and Lindahl, E.G., Emission of inertial waves by baroclinically unstable flows: laboratory experiments with Altimetric Imaging Velocimetry. *J. Atmos. Sci.* 2008, **65**, 250–262.

Broomhead, D.S. and King, G.P., Extracting qualitative dynamics from experimental data. *Physica D* 1986, **20**, 217–236.

Daniels, P.G., Stationary instability of the buoyancy-layer flow between heated vertical planes. *Proc. R. Soc. Lond.* 1985, **401**, 145–161.

Farnell, L. and Plumb, R.A., Numerical integration of flow in a rotating annulus: axisymmetric model. *Geophysical Fluid Dynamics Laboratory, UK Meteorological Office* 1975, **Unpublished**.

Farnell, L. and Plumb, R.A., Numerical integration of flow in a rotating annulus: three dimensional model. *Geophysical Fluid Dynamics Laboratory, UK Meteorological Office* 1976, **Unpublished**.

Ford, R., McIntyre, M.E. and Norton, W.A., Balance and the slow quasimanifold: some explicit results. *J. Atmos. Sci.* 2000, **57**, 1236–1254.

Fowlis, W.W. and Hide, R., Thermal convection in a rotating annulus of liquid: effect of viscosity on the transition between axisymmetric and non-axisymetric flow regimes. *J. Atmos. Sci.* 1965, **22**, 541–558.

Früh, W.G. and Read, P.L., Wave interactions and the transition to chaos of baroclinic waves in a thermally driven rotating annulus. *Phil. Trans. R. Soc. London* 1997, **355**, 101–153.

Ghil, M., Allen, M.R., Dettinger, M.D., Ide, K., Kondrashov, D., Mann, M.E., Robertson, A.W., Saunders, A., Tian, Y., Varadi, F. and Yiou, P., Advanced spectral methods for climatic time series. *Rev. Geophys.* 2002, **40**, 1–41.

Gill, A.E., The boundary-layer regime for convection in a rectangular cavity. *J. Fluid Mech.* 1966, **26**, 515–536.

Gill, A.E. and Davey, A., Instabilities of a buoyancy-driven system. *J. Fluid Mech.* 1969, **35**, 775–798.

Hide, R. and Mason, P.J., Sloping convection in a rotating fluid. *Adv. in Phys.* 1975, **24**, 47–100.

Hignett, P., White, A.A., Carter, R.D., Jackson, W.D.N. and Small, R.M., A comparison of laboratory measurements and numerical simulations of baroclinic wave flows in a rotating cylindrical annulus. *Q. J. R. Meteorol. Soc.* 1985, **111**, 131–154.

James, I.N., Jonas, P.R. and Farnell, L., A combined laboratory and numerical study of fully developed steady baroclinic waves in a cylindrical annulus. *Q. J. R. Meteorol. Soc.* 1981, **107**, 51–78.

Knox, J.A., McCann, D.W. and Williams, P.D., Application of the Lighthill-Ford theory of spontaneous imbalance to clear-air turbulence forecasting. *J. Atmos. Sci.* 2008, **65**.

Leith, C.E., Nonlinear normal mode initialization and quasi-geostrophic theory. *J. Atmos. Sci.* 1980, **37**, 958–968.

Lorenz, E.A., Attractor sets and quasi-geostrophic equilibrium. *Q. J. R. Meteorol. Soc.* 1980, **37**, 1685–1699.

Lovegrove, A.F., Read, P.L. and Richards, C.J., Generation of inertia-gravity waves in a baroclinically unstable fluid. *Q. J. R. Meteorol. Soc.* 2000, **126**, 3233–3254.

Lynch, P., Resonant motions of the three-dimensional elastic pendulum. *Int. J. Non. Lin. Mech.* 2002, **37**, 345–367.

McIntyre, M.E., Balanced flow. *Encyclopedia of Atmos. Sciences; ed. J. R. Holton, J. A. Pyle and J. A. Curry* 2003, **2**, 680–685.

Plougonven, R., Teitelbaum, H. and Zeitlin, V., Inertia gravity wave generation by the tropospheric mid

latitude jet as given by the Fronts and Atlantic Storm-Track Experiment radio soundings. *J. Geophys. Res.* 2003, **108**.

Read, P.L., Applications of singular systems analysis to 'baroclinic chaos'. *Physica D* 1992, **58**, 455–468.

Richardson, L.F., Weather prediction by numerical process. *Cambridge University Press* 1922 Reprinted by Dover Publications, New York, 1965.

Warn, T. and Menard, R., Nonlinear balance and gravity-inertial wave saturation in a simple atmospheric model. *Tellus* 1986, **38**, 285–294.

Williams, P.D., Haine, T.W.N. and Read, P.L., On the generation mechanisms of short-scale unbalanced modes in rotating two-layer flows with vertical shear. *J. Fluid Mech.* 2005, **528**, 1–22.

Williams, P.D., Haine, T.W.N. and Read, P.L., Inertia-gravity waves emitted from balanced flow: observations, properties and consequences. *J. Atmos. Sci.* 2008, **65**, 3543–3556.

Williams, P.D., Read, P.L. and Haine, T.W.N., Spontaneous generation and impact of inertia-gravity waves in a stratified, two-layer shear flow. *Geophys. Res. Lett.* 2003, **30**, 2255.

Young, R.M.B. and Read, P.L., Flow transitions resembling bifurcations of the logistic map in simulations of the baroclinic rotating annulus. *Physica D* 2008, **237**.

Zhang, F., Generation of mesoscale gravity waves in upper-tropospheric jet-front systems. *J. Atmos. Sci.* 2004, **61**, 440–457.